

# The Proximity Effect on the Lyman $\alpha$ Forest due to a foreground QSO

A. Fernández-Soto<sup>1</sup>, X. Barcons<sup>2</sup>, R. Carballo<sup>1</sup>, J.K. Webb<sup>3</sup>

<sup>1</sup> *Departamento de Física Moderna, Universidad de Cantabria. 39005, Santander, Spain*

<sup>2</sup> *Instituto de Física de Cantabria.*

*Consejo Superior de Investigaciones Científicas - Universidad de Cantabria. 39005, Santander, Spain*

<sup>3</sup> *Kensington School of Physics. University of New South Wales. Sydney, Australia.*

Accepted 1995 June 7. Received 1995 February 27; in original form 1994 October 11

## ABSTRACT

The influence of a foreground QSO on the Lyman  $\alpha$  forest of another QSO with higher redshift has been investigated by analyzing the spectra of three such objects at redshifts  $z = 2 - 2.7$ . This influence is not contaminated by any projection effects, as opposed to the inverse effect along the line of sight, where incomplete coverage of the QSO continuum emitting region by the Lyman  $\alpha$  clouds could contribute to the relative lack of lines. Our results are consistent with the existence of a proximity effect due to the foreground QSO, but due to its weakness we can only reject the absence of such effect at  $\sim 1\sigma$  level. By modelling this proximity effect assuming that Lyman  $\alpha$  clouds are low-density highly ionized objects we find that the best value for the UV photoionizing intensity at those redshifts is  $\sim 10^{-20.5} \text{ erg cm}^{-2} \text{ s}^{-1} \text{ Hz}^{-1} \text{ srad}^{-1}$  at the Lyman limit which is consistent with previous estimates of the background based on the inverse effect. We also find an absolute lower limit (at 95 per cent confidence) to the UV intensity at the level of  $10^{-21.8} \text{ erg cm}^{-2} \text{ s}^{-1} \text{ Hz}^{-1} \text{ srad}^{-1}$  which means the rejection of a number of models for the UV background where it is mostly contributed by QSOs, and absorption by Lyman limit systems is taken into account.

**Key words:** Intergalactic medium – quasars: absorption lines – quasars : individual 1055+021 – quasars : individual 1222+228 – quasars : individual 1228+077.

## 1 INTRODUCTION

The inverse effect in the redshift distribution of the Lyman  $\alpha$  absorption lines seen towards distant QSOs (which is a relative lack of these lines at redshifts close to the QSO one) was first detected by Weyman, Carswell & Smith (1981). It was soon realized that different values were obtained for the evolution parameter  $\gamma$  when trying to fit a power law to the number density of lines per unit redshift,

$$\frac{dN}{dz} = A(1+z)^\gamma \quad (1)$$

depending on whether a single QSO was taken or a sample of them was used. The fit of such form to any single QSO always resulted in lower values of  $\gamma$  than when several QSO samples were considered as a whole (Carswell et al. 1982). Murdoch et al. (1986) explored this effect with a large sample of Lyman  $\alpha$  lines obtained from intermediate-to low- resolution spectroscopy of several QSOs, concluding that there was a relative decrease in the line number density when the absorption redshift approached the emission redshift. Tytler (1987), by using a larger but more inhomogeneous sample, reached a similar conclusion, except for the fact that he claimed that the inverse effect (or anomaly) was detected far away from the observed QSO, whilst Murdoch et al (1986) concluded that this effect was restricted to a distance  $\sim 8 h_{50}^{-1}$  from the QSO. Webb & Larsen (1988), in a detailed analysis of a large sample, also concluded that the inverse effect was concentrated at a short distance from the observed QSO.

Several models have been suggested to explain the inverse effect. The first one invokes some sort of local mechanism around the observed QSO that renders undetectable the Lyman  $\alpha$  clouds close to it, for example in terms of enhanced photoionization by the QSO (Murdoch et al. 1986; Tytler 1987; Bajtlik, Duncan & Ostriker 1988, hereafter BDO). Another class of models postulates a rather small size for the Lyman  $\alpha$  clouds, in such a way that at redshifts close to the QSO they are unable to cover its continuum emitting region, resulting in a relative lack of lines above any given threshold (Tytler 1987). Finally Lu, Wolfe & Turnshek (1991) tested whether a flattening of the power law (1) at high redshift could explain the inverse effect. Although these

authors find some evidence for this flattening, they conclude that it does not remove the inverse effect at all.

If the photoionization explanation for the inverse effect is to be assumed real, the Lyman  $\alpha$  clouds would be galaxy-sized objects, with a rather low density  $n_H < 10^{-4} \text{ cm}^{-3}$  and a high ionization fraction  $n_{\text{HII}}/n_{\text{HI}} \sim 10^5$ . Collisional ionization would then be negligible and the optically thin gas would therefore be mostly ionized by the UV photons from the general background plus the ones contributed by any nearby QSO. If, on the contrary, the reason for the inverse effect is the small size of the Lyman  $\alpha$  clouds, these objects would have large densities ( $n_H > 1 \text{ cm}^{-3}$ ), they would be almost neutral (except for a small fraction of collisionally ionized atoms) and photoionization by UV photons would be less important. All the models described above present some problems. For the second class of models the Lyman  $\alpha$  clouds should be very small ( $\sim pc$  size) in contradiction with the compelling evidence that they have a size similar to a galaxy (Hippelein & Meisenheimer 1993) or even larger (Smette et al. 1992; Dinshaw et al. 1994; Bechtold et al. 1994). These models also require an unphysical fine tuning of the cloud size and the QSO continuum emitting region (Barcons & Fabian 1987). On the other hand, the photoionization model predicts a correlation between the magnitude of the inverse effect and the ionizing flux from the QSO, a fact whose observational confirmation is still unclear (Barcons & Fabian 1987; Webb & Larsen 1988; Lu et al. 1991; Bechtold 1994).

Therefore, the present situation is that the most likely explanation for the inverse effect is that the enhanced photoionization field around the QSO evaporates or overionizes the surrounding clouds.

In order to provide a complementary test for the local (photoionization) models, we have searched for the possible effect introduced in the Lyman  $\alpha$  forest of a background QSO by a foreground QSO which lies close to the line of sight under study. If the inverse effect is due to the photoionization from the QSO, in our situation, the foreground object should also influence the Lyman  $\alpha$  forest of the background QSO. If, on the contrary, the small size of the clouds is the reason for the inverse effect, we should not detect any influence from the foreground QSO. Similar works have been presented previously by Crofts (1989) and Dobrzycki & Bechtold (1991).

After having studied three such cases, we have only been able to marginally detect what we shall call the *proximity effect* (following the suggestion by BDO) at  $\sim 1\sigma$  confidence. Subsequent modelling of this effect enables us to estimate the general UV ionizing background for which we have a result entirely consistent with estimates based on the inverse effect itself. Under the photoionization scheme, we find firm lower limits to the UV ionizing background which enable us to reject some of the models that have been put forward to account for the high- $z$  UV intensity.

The paper is organised as follows. Section 2 presents the objects selected for our study and a summary of the observations. In Sections 3 and 4 we discuss with detail the absorption line lists obtained by line fitting the spectra of the three objects used. Much attention is devoted to identifying the heavy-element systems (Section 3) in order to remove any lines in the Lyman  $\alpha$  forest that do not correspond to Lyman  $\alpha$  clouds. Some discussion on the distribution of the

**Table 1.** The observed QSO pairs.

OBJECT	COORDINATES		$^a$ $m_V$	$z$	$\theta^b$
	$\alpha$	$\delta$			
1055+021	10 57 57	01 54 03	17.8	2.73	
1055+021	10 57 13	01 47 55	20.0	2.29	12.6
1222+228	12 25 27	22 35 13	15.5	2.051	
1222+228	12 25 24	22 31 28	19.0	1.87	3.8
1228+077	12 31 21	07 25 18	17.6	2.391	
1228+077	12 31 08	07 24 39	17.5	1.878	5.7

$^a$  J2000

$^b$  Angular separation between lines of sight, in arcmin

clouds is also presented based on our data in Section 4. In Section 5, we explain and perform the test for the proximity effect after modelling it in terms of a simple photoionization model. Section 6 presents a brief discussion of our findings, and implications for the origin of the high redshift UV background.

## 2 THE DATA

### 2.1 The Sample

A search has been made in the Hewitt and Burbidge Catalogue (Hewitt & Burbidge 1993) for every pair of QSOs matching the following conditions:

- (i) The background QSO (redshift  $z_b$ ) must have a significant part (at least  $40000 \text{ km s}^{-1}$ ) of its Lyman  $\alpha$  forest (i.e., the spectral region contained between the Lyman  $\alpha$  and Lyman  $\beta$  emission lines) in the visible region of the spectrum ( $\lambda > 3250 \text{ \AA}$ ).
- (ii) The foreground QSO must have a redshift ( $z_f$ ) such that it is able to influence the visible fraction of the Lyman  $\alpha$  forest of the background QSO, i.e.,  $1216(1+z_f) \text{ \AA}$  must fall within the observable Lyman  $\alpha$  forest of the background object *and* be further than  $5000 \text{ km s}^{-1}$  from  $1216(1+z_b) \text{ \AA}$  in order to avoid overlapping of the inverse effect and the proximity effect we are looking for.
- (iii) The magnitude of the background QSO should be  $\leq 18$ , so that spectroscopy at moderate resolution can be easily obtained.
- (iv) The angular separation between both QSOs should be less than 20 arcmin, which corresponds to  $\sim 10 h_{50} \text{ Mpc}$  at  $z \sim 2.5$ . Here, and throughout this paper, we use the standard cosmology parameters  $q_0 = 0.5$  and  $H_0 = 50 h_{50} \text{ km s}^{-1} \text{ Mpc}^{-1}$ .

The selection process produced a preliminary sample containing about 30 such pairs. After another filtering process, based on use of other catalogues to avoid misclassified objects and possibilities of observation from the Observatorio del Roque de los Muchachos at La Palma (Canary Islands, Spain), we obtained a reduced target sample with 10 QSO pairs.

All through this paper, each pair will be named according to the name of the background QSO. Two of our pairs (1307+296 and 1305+298) turned up to be stars, as was seen

by taking short-exposure spectra at low resolution with the William Herschel Telescope in 1993 February.

The sample that we observed, consisting of three QSOs is shown in Table 1. These QSOs span a rather restricted redshift range ( $z = 2 - 2.7$ ) but cover a wider range in terms of angular separations from the foreground QSO ( $\theta = 3.8 - 12.6$ ). That will allow us to test the existence of the proximity effect under different circumstances (see Section 5).

## 2.2 Observations and data reduction

All observations were performed at the Observatorio del Roque de los Muchachos in the island of La Palma (Canary Islands, Spain). Data from QSO1228+077 were acquired using the Isaac Newton Telescope with the IDS spectrograph and IPCS (Image Photon Counting System) detector in 1989 February. The data from QSO1222+228 were taken in 1993 February, using the William Herschel Telescope with the ISIS double spectrograph and the IPCS-II as detector in the blue arm. Finally, data from QSO1055+021 were taken in 1994 February, again using the ISIS double spectrograph and the TEK/CCD detector on the blue arm of the same telescope. A reduced version of the observing logs is listed in Table 2.

The choice of the IPCS and IPCS-II to observe QSO1228+077 and QSO1222+228 was done because the crucial part of the spectrum (i.e., the part putatively influenced by the foreground QSO) falls at  $\lambda < 4000 \text{ \AA}$  where this detector has better sensitivity than any of the available CCDs at La Palma.

The blue gratings were chosen in order to have an approximate reciprocal resolution of about  $\sim 0.2 \text{ \AA}/\text{pixel}$ . This produced a spectral resolution good enough to allow profile fitting of the absorption lines present in the different spectra.

Although we tuned the red arm settings of the ISIS double spectrograph (during the observations of QSO1222+228 and QSO1055+021), in order to identify metal lines of possible heavy-element absorption systems with associated Lyman  $\alpha$  lines falling in the blue arm region, we did not find any line that either confirmed or rejected any possible system.

The data reduction was carried out using the Starlink FIGARO package. We used standard techniques, except that we needed to generate and propagate through the entire process an error array for which we had to make the suitable modifications to the standard routines provided by FIGARO. To obtain a precise wavelength-scale, calibration arc lamps were exposed before and after each integration on all of our objects. Heliocentric and air-to-vacuum corrections were performed. No attempt has been made to obtain a flux calibration for any of the QSOs, which does not affect to the parameters of the absorption lines.

As it can be seen from Table 2, the data from QSO1055+021 are of a much higher quality, caused by the longer exposure time and better sky conditions during their acquisition. None the less, data from all three QSOs have spectral resolution and signal-to-noise ratio good enough to perform absorption line fitting.

Continuum fitting was carried out using a standard spline method. Selected regions of each spectrum were used in an iterative way that rejected in each iteration the points

that were significantly deviant from the fitted continuum, until the fitting procedure converged.

A preliminary absorption line list was obtained searching for significant (greater than  $4\sigma$ ) deviations from the continuum in the normalized spectra, following the method presented in Young et al. (1979).

Voigt profiles were fitted to each line (or blend of lines) in the spectra using the absorption line fitting code ALF developed by ourselves. This program performs  $\chi^2$  minimisation of a spectral region by introducing a Voigt profile for each line (that is why the error array is needed). The program finds the best-fitting column density, Doppler dispersion parameter and redshift for each one of the lines, assuming that they correspond to given ions and atomic transitions. ALF also produces an estimate of the errors on these parameters and a goodness-of-fit given the minimum  $\chi^2$  reached and the number of degrees of freedom. A fit was considered to be good enough if it is not rejected by more than 99 per cent probability, according to  $\chi^2$  statistics. If the fit over a selected region was not good enough, another line (with free column density, velocity dispersion parameter and redshift) was added and the fit repeated. The process was stopped either when the rejection probability is less than 99 per cent and the fit looked good to the eye, or when addition of a new line resulted in an *increase* of the rejection probability. This avoids overfitting to a large extent. The resulting line lists are presented in Table 3 (QSO1055+021), Table 4 (QSO1222+228) and Table 5 (QSO1228+077).

In Figures 1, 2 and 3 we show the spectra of the 3 objects QSO1055+021, QSO1222+228 and QSO1228+077 respectively, with arrows marking the wavelength of the Lyman  $\alpha$  emission line for each respective foreground QSO. These spectra have been normalized to the fitted continuum. The spectral fit achieved is also shown as a dotted line. There are several features in these spectra that we do not believe to be absorption lines, since their width is too small for the spectral resolution we have obtained. In fact we tried to fit these ‘lines’ and found that the absence of a line provided a better fit than the presence of an absorption line. The most conspicuous of these features, which we believe to be spikes of the noise, appear around 4010 and 4108  $\text{\AA}$  in Fig. 1, and in 3487 and in 3762  $\text{\AA}$  in Fig. 3.

## 3 THE HEAVY-ELEMENT ABSORPTION SYSTEMS

A fraction of the absorption lines observed in QSO spectra are supposed to be caused by absorption from elements other than H I. These are the so-called metal lines, which have their origin in systems rich in metals and are called heavy-element absorption systems.

In order to search for heavy-element absorption systems in our list, we cross-correlated it with a list of the most relevant atomic transitions following the method by Young et al. (1979). We used the same ‘short list’ as in their paper, with some additions in order to make it denser in certain wavelength ranges. The new added lines are CI  $\lambda 1261$ , AlII  $\lambda 1670$ , AlIII  $\lambda \lambda 1854, 1862$ , MgI  $\lambda 2026$ , BeII  $\lambda 3131$ , NaI  $\lambda 3303$ , AlI  $\lambda \lambda 3083, 3093$  and CaI  $\lambda 4227$ .

As a result of this correlation analysis, a function representing the number of coincidences of different lines with the

**Table 2.** Summary of observations.

OBJECT	INSTRUMENT	DATE	WAVELENGTH RANGE (Å)	EXP. TIME (h)	SEEING (arcsec)	$\sigma_v^a$ ( $\text{km s}^{-1}$ )	S/N <sup>b</sup>
1055+021	WHT+ISIS+TEK/CCD	13-Feb-94	3910 - 4111	3.3	1	13.2	9-13
1222+228	WHT + ISIS + IPCS-II	14-Feb-93	3255 - 3695	1.1	1.5		
1222+228	WHT + ISIS + IPCS-II	15-Feb-93	3255 - 3695	1.7	2	36.3	6-12
1228+077	INT + IDS + IPCS	8-Feb-89	3360 - 3845	2.8	1.5		
1228+077	INT + IDS + IPCS	9-Feb-89	3360 - 3845	5.0	1.5	34.1	4-7

<sup>a</sup> Dispersion of the spectrum.

<sup>b</sup> Minimum and maximum signal-to-noise ratio as estimated from the spectra.

same absorption system redshift is obtained. The peaks of this cross-correlation function are prime candidates for correspondance to heavy-element systems. In order to assess the significance of these peaks, we generated 100 synthetic line lists uniformly distributed over the available wavelength range for each spectrum, and performed the same cross-correlation analysis. Averaging of these 100 cross-correlation functions provided a measure of the noise level for the function corresponding to the real data. All the peaks of the cross-correlation function above  $1\sigma$  were carefully studied using the complete line list obtained by the line fitting procedure rather than from the preliminary list produced by FIGRED. Special attention was payed to multiplet transitions of MgII, CIV, SiII, SiIV and AlIII. We considered that a putative heavy-element system is real if it matches the following conditions:

- (i) A system with  $\lambda_{min} \leq 1215.67(1 + z_{abs}) \leq \lambda_{max}$  was accepted only if its Lyman  $\alpha$  line was present (the spectrum ranges from  $\lambda_{min}$  to  $\lambda_{max}$  and  $z_{abs}$  is the redshift of the possible absorption system).
- (ii) In the case of reasonably unblended multiplets, their line ratios should be consistent with the expected values.
- (iii) Every system with a column density for any ion larger than the one for the associated Lyman  $\alpha$  line was rejected.

These criteria effectively ensured the rejection of many of the candidate heavy-element absorption systems. With all of the selected systems, we used a more complete list of atomic transitions (in fact a list that contains all transitions ever detected in QSO absorption system work) to search for extra coincidences in the spectrum at the absorption system redshift.

The identification of heavy-element systems is particularly difficult in the spectrum of QSO1055+021, because of the small spectral coverage. In this and the other objects we have accepted as a heavy-element system anyone that fulfils the above criteria, even if some of the lines are blended with absorption lines from other systems, when the reality of such metal system casts some doubts. However, we have taken these systems as real, since we prefer to get the Lyman  $\alpha$  line lists as clean as possible from any contamination. To make sure that this decision will not affect the main goal of this work, we checked that the wavelengths at which these doubtful systems appear are far from the spectral regions in which the proximity effect from the foreground QSO will be important, which is fortunately the case.

This is the (perhaps overcomplete) final list of heavy-element systems in the spectra. There are previously reported spectra and line lists for QSO1228+077 (Robertson & Shaver 1983) and QSO1222+228 (Bahcall, Osmer & Schmidt 1969; Morton & Morton 1972; Bechtold et al. 1984) that have lower spectral resolution. We also compare our findings with these works.

### 3.1 QSO1055+021

$z = 2.14469 \pm 0.00003$ . The only important observable lines within the wavelength range are SiII  $\lambda\lambda 1260, 1304$ . Both are detected, but the second one is blended.

$z = 2.32935 \pm 0.00002$ . Observed Lyman  $\alpha$  and SiIII  $\lambda 1206$  lines. No other line is detected, although SiII  $\lambda\lambda 1260, 1304$  fall within the observed range.

$z = 1.14360 \pm 0.00011$ . The only lines within the observed spectral range are AlIII  $\lambda\lambda 1854, 1862$ ; and both are detected and in good agreement with theoretical line ratio although the second one is blended.

$z = 0.31469 \pm 0.00003$ . This is the most dubious system for this QSO. The only available lines are AlI  $\lambda\lambda 3083, 3093$ . Both are detected, and the line ratio is correct, but the second one blends slightly with another Lyman  $\alpha$  line.

$z = 1.37569 \pm 0.00007$ . The red spectrum suggests the possibility of another metal system, at  $z = 1.37569 \pm 0.00007$ . This is based upon a possible CaII doublet  $\lambda\lambda 3934, 3969$ . No other line with this redshift could be detected in the available wavelength range (both blue and red arms) to confirm or reject this possibility, as we do not trust the absence of AlII  $\lambda 1671$  in the blue arm spectrum as a safe test to reject this system.

### 3.2 QSO1222+228

$z = 1.93724 \pm 0.00007$ . This is a really interesting system. Its existence has been first reported by Bahcall et al. (1969). In addition Morton & Morton (1972) also reported the presence of structure in the absorption lines. We can confirm the presence of three subsystems, with redshifts  $1.93606 \pm 0.00013$  (A),  $1.93724 \pm 0.00007$  (B) and  $1.93853 \pm 0.00007$  (C), with a high degree of confidence: Lyman  $\alpha$  lines, together with the doublet NV  $\lambda\lambda 1238, 1242$  are seen for all three subsystems, and the line SiIII  $\lambda 1206$  has been fitted for subsystems B and C. We do not believe that the lack of

SiII  $\lambda\lambda 1190, 1193$  is a relevant problem. The computed  $\Delta v$  for subsystems A and C with respect to subsystem B are  $121 \pm 39$  and  $132 \pm 29 \text{ km s}^{-1}$ .

- (ii)  $z = 1.23238 \pm 0.00005$ . The CIV  $\lambda\lambda 1548, 1550$  doublet is present (the second component is blended). We have also detected a line of CI  $\lambda 1560$  and FeII  $\lambda 1608$ . The only remaining line in the range, SiII  $\lambda 1527$ , is not detected.
- (iii)  $z = 2.03669 \pm 0.00005$ . Lyman  $\alpha$  and SiII  $\lambda\lambda 1190, 1193$  are seen, although the second line of this doublet is blended. SiIII  $\lambda 1206$  is absent.
- (iv)  $z = 1.51408 \pm 0.00006$ . SiIV  $\lambda\lambda 1394, 1403$  and CII  $\lambda 1335$  are detected. No SiII  $\lambda 1304$  absorption line is seen.
- (v)  $z = 0.47372 \pm 0.00003$ . Three lines of the FeII multiplet  $\lambda\lambda 2344, 2375, 2383$  are seen. No other line is –nor should be– observed in this wavelength range.
- (vi)  $z = 0.40722 \pm 0.00011$ . Another system characterised by four FeII lines. In this case, wavelengths are  $\lambda\lambda 2344, 2383, 2587$  and  $2600$ .
- (vii)  $z = 0.23807 \pm 0.00004$ . This is a MgII  $\lambda\lambda 2796, 2803$  doublet. The first component is blended. MgI  $\lambda 2853$  is not seen.
- (viii)  $z = 0.26986 \pm 0.00003$ . Another MgII doublet. The first component is slightly blended. Two FeII lines and MgI  $\lambda 2853$  are absent.
- (ix)  $z = 0.29962 \pm 0.00005$ . Yet another proposed MgII doublet. The second component is blended. FeII lines are not detected.
- (x)  $z = 1.92307 \pm 0.00004$ . Dubious SiII  $\lambda\lambda 1190, 1193$  and clear SiII  $\lambda 1260$  line with correct line ratios. The associated Lyman  $\alpha$  line is slightly blueshifted ( $30 \text{ km s}^{-1}$  away) but is still consistent given the spectral resolution.

In comparison with previously available lists, we can say that the  $z=1.93727$  system has been totally confirmed, as well as its structure. We can also report the detection of a Lyman  $\alpha$  line at  $z=1.98095 \pm 0.00003$ , that matches the CIV doublet reported by Sargent et al. (1988) at  $z=1.9805$  –also noticed as Lyman Limit system by Bechtold et al. (1984).

### 3.3 QSO1228+077

- (i)  $z = 1.89678 \pm 0.00005$ . This is a very clear heavy-element system. We have detected its Lyman  $\alpha$  line, SiII  $\lambda\lambda 1190, 1193$ , SiII  $\lambda\lambda 1260, 1304$ , and SiIII  $\lambda 1206$ . This means that all important lines in our wavelength range have been detected.
- (ii)  $z = 2.01967 \pm 0.00006$ . Detected Lyman  $\alpha$  absorption, together with SiIII  $\lambda 1206$ . There is no sign of the SiII  $\lambda\lambda 1190, 1193$  and  $1260$  lines.
- (iii)  $z = 2.13687 \pm 0.00004$ . As in (ii), we detect Lyman  $\alpha$  and SiIII  $\lambda 1206$ . SiII  $\lambda\lambda 1190$  and  $1193$  are absent.
- (iv)  $z = 2.29915 \pm 0.00013$ . A dubious system, marked by the presence of Lyman  $\beta$  and CII  $\lambda 1036$  absorption. There is no other line in this region of the spectrum to aid a decision.
- (v)  $z = 1.20687 \pm 0.00007$ . The CIV  $\lambda\lambda 1548, 1551$  doublet is detected. The line ratio is correct, and the lines are only slightly blended.

The first three listed absorption systems of this QSO correspond to systems A, B and C by Robertson & Shaver (1983). Thus, we can confirm the presence of B and C, which Robertson & Shaver (1983) left as ‘probable’.

A very strong line in the spectrum of Robertson & Shaver (1983) at  $4010.4 \text{ \AA}$  is likely to correspond to the Lyman  $\alpha$  line associated with the system (iv) at  $z = 2.29915$ .

## 4 THE LYMAN $\alpha$ LINES

All the absorption lines not belonging to any of the above heavy-element systems and falling in the QSO Lyman  $\alpha$  forest are identified as Lyman  $\alpha$  absorption lines. From the process presented in the previous section we can conclude that the contamination from lines belonging to heavy-element absorption systems is, if it exists at all, minimal. Since for all of the absorption lines we have the column density, the Doppler dispersion parameter and the redshift (together with the corresponding error estimates) we can in principle obtain the distribution of these quantities. Some of them will, in fact, be needed to properly model the strength of the proximity effect produced by the foreground QSO.

### 4.1 The column density distribution

A first inspection of the column density distribution of the Lyman  $\alpha$  absorption systems for the three QSOs reveals that our lists are complete down to (at least)  $N_{HI} \approx 7 \times 10^{13} \text{ cm}^{-2}$  in the case of the QSOs 1222+228 and 1228+077, while we believe  $N_{HI} \approx 10^{13} \text{ cm}^{-2}$  to be our completeness limit for the improved resolution better signal-to-noise spectrum of QSO1055+021. Although all of the analysis that we present here is based on a column-density-limited sample, we can use our  $N_{HI}$  cut-off together with a typical value for  $b$  ( $35 \text{ km s}^{-1}$ ) and derive an equivalent width cut-off of  $\simeq 0.25 \text{ \AA}$ . We remark that this limit is merely orientative and does not imply any use of the equivalent widths of the lines in the rest of this work.

As usual, a single power law has been fitted to the column density distribution

$$p_N(N_{HI}) \propto N_{HI}^{-\beta}, \quad (2)$$

via maximisation of the likelihood function which does not require the binning up of the data. In the case of QSO1055+021, for which we have a relatively small spectral coverage, there are two lines with large column density ( $N_{HI} > 8 \times 10^{15} \text{ cm}^{-2}$ ) for which we have no way of testing whether or not they have associated metals. Since we have strong suspicions that they could in fact belong to heavy-element systems, we prefer to fit the column density distribution for this QSO up to a maximum column density  $N_{HI} < 8 \times 10^{15} \text{ cm}^{-2}$ .

Fitting the column density distribution down to  $N_{HI} > 7 \times 10^{13} \text{ cm}^{-2}$  to the absorption lines of each QSO separately produces results that are consistent with the standard value usually found in the literature ( $\beta \approx 1.7$ ; see Table 6 for details). It is also worth mentioning that the column density distribution for the lines in QSO1055+021 reveals a flatter slope when the fit to the data from this QSO is performed down to  $N_{HI} = 10^{13} \text{ cm}^{-2}$  ( $\beta = 1.55_{+0.13}^{-0.12}$ ). This might be a result of the fact that the  $p_N(N_{HI})$  flattens below some column density, as it was reported by Carswell et al. (1987) and also indirectly inferred by Webb et al. (1992).

By fitting the whole sample together the maximum likelihood method yields  $\beta = 1.70_{-0.09}^{+0.08}$ . This is the value that will be used in Section 5.

**Table 3.** Fits to the Lyman  $\alpha$  absorption lines distribution.

OBJECT	$N_{HI}^{inf a}$	$N_{HI}^{sup b}$	$\beta$	$\bar{b}$	$\sigma_b$	$A$
1055+021	$1.10^{13}$	$\infty$	$1.77^{+0.32}_{-0.25}$	$26.5^{+3.5}_{-3.5}$	$15.5^{+2.5}_{-2.5}$	$10.7 \pm 2.5$
1222+228	$7.10^{13}$	$\infty$	$1.77^{+0.17}_{-0.15}$	$48.5^{+12.5}_{-12.5}$	$30^{+11}_{-7}$	$7.0 \pm 1.6$
1228+077	$7.10^{13}$	$\infty$	$1.70^{+0.13}_{-0.11}$	$70^{+18}_{-18}$	$55^{+15}_{-9}$	$8.6 \pm 1.6$
Sample Average	$7.10^{13}$	$\infty$	$1.70^{+0.08}_{-0.09}$	—	—	$8.5 \pm 1.0$

<sup>a</sup> Lower column density limit used in calculations.

<sup>b</sup> Upper column density limit used in calculations.

## 4.2 The distribution of Doppler dispersion parameters

As usual we have fitted a Gaussian form to the distribution of the  $b$  parameter

$$p_b(b) = \frac{1}{\sigma_b \sqrt{2\pi}} \exp\left(-\frac{(b - \bar{b})^2}{2\sigma_b^2}\right) \quad (3)$$

Because of the lower resolution and signal to noise ratio, data from QSO1222+228 and 1228+077 have a poorer definition in the measurements of the Doppler dispersion parameter  $b$ . To avoid contamination from badly determined  $b$ s, we have removed from the fitting procedure all lines with  $b$  determined with an error larger than  $100 \text{ km s}^{-1}$ .

The results are listed in Table 6. The lower spectral resolution data (QSO1222+228 and 1228+077) produce larger  $\bar{b}$  values and dispersions than expected. This difference can be understood as an artifact of the resolution itself – it is very difficult to detect lines much narrower than the resolution. When it is low, as in the QSO1222+228 and 1228+077 cases, the fitted values reflect more the spectral resolution itself than the intrinsic distribution of the line Doppler dispersions. This is also reflected in the error estimates of the  $\bar{b}$  and  $\sigma_b$  parameters, which have been obtained by using the likelihood function as a probability density in parameter space. These errors are clearly larger for the low resolution data, which implies a poorer determination, caused by line blending in the spectra.

## 4.3 The redshift distribution

The redshift distribution of lines,  $\frac{dN}{dz}$ , is also required to model the proximity effect. Our idea is basically to use the standard power-law distribution (equation 1), and correct it according to the relative influence of the background and foreground QSOs. But to do this, we must first make sure that our sets of lines are compatible with the coefficients that we will use,  $A$  and  $\gamma$ . For example, Webb et al. (1992), use  $A_o = 11.6$  and  $\gamma_o = 1.987$  for lines with column density greater than  $7 \times 10^{13} \text{ cm}^{-2}$  which appears to be appropriate for intermediate to high resolution studies.

Unfortunately, it is not possible to perform an accurate  $\gamma$  fitting in such a short redshift range and with such restricted wavelength coverage in each spectrum. For this reason we computed the value of  $A$  for each QSO taking  $\gamma = \gamma_o$  fixed. The results are also listed in Table 6, together with an error estimated in terms of Poisson counting statistics over the redshift range covered. The values of  $A$  are consistent

with the  $A_o$  value quoted in the literature. The overall value for the normalisation is  $A = 8.5 \pm 1$ , which is the value that we shall use in the next Section.

## 5 PHOTOIONIZATION OF THE LYMAN $\alpha$ FOREST BY A FOREGROUND QSO

### 5.1 Modelling the Proximity Effect by a nearby QSO

As explained in the Introduction, the inverse effect (in our case the proximity effect) is most likely as result of an enhancement of the UV ionizing field in the neighbourhood of a QSO which consequently increases the ionization fraction of the Lyman  $\alpha$  clouds. Although other models with similar philosophy may also explain the inverse effect (for example gravitational infall of the Lyman  $\alpha$  clouds onto the QSO), we have modelled the proximity effect in terms of photoionization of low-density highly ionized clouds of gas – much similar to the way that BDO modelled the inverse effect but including the ionization from the foreground QSO.

The basic idea is that for a highly ionized plasma, where collisional ionization can be ignored, the neutral gas density is inversely proportional to the total UV ionizing intensity. If  $J_o$  is the general UV background intensity (in  $\text{erg cm}^{-2} \text{ s}^{-1} \text{ Hz}^{-1} \text{ rad}^{-1}$ ) at the local Lyman limit frequency, and  $F_Q$  is the UV flux (in  $\text{erg s}^{-1} \text{ cm}^{-2} \text{ Hz}^{-1}$ ) produced by a QSO located at a distance  $d_Q$  from the Lyman  $\alpha$  cloud, the HI column density will be reduced by the presence of the QSO according to

$$N_{HI} \propto (4\pi J_o + F_Q)^{-1} \propto (1 + \omega_Q)^{-1}. \quad (4)$$

where

$$\omega_Q = \frac{F_Q}{4\pi J_o}. \quad (5)$$

The flux of the QSO on the Lyman  $\alpha$  cloud is just  $L_Q/(4\pi d_Q^2)$  where  $L_Q$  is the QSO luminosity at the local Lyman limit frequency and  $d_Q$  is the distance from the QSO to the Lyman  $\alpha$  cloud. We have estimated  $L_Q$  in the same way as Tytler (1987), by using the measured V magnitude and a suitable  $K$  correction. We have used the  $K$  correction presented by Evans & Hart (1977), assuming that it holds up to a redshift of 2.7. We have also assumed that the emission from the foreground QSO is isotropic (i.e., no beaming) and that the measured magnitude has not been seriously contaminated by gravitational lensing or micro-lensing amplification along the line of sight. Another implicit assumption

in this framework is that the foreground QSO luminosity is not variable. We will discuss this point further in Section 6.

Within this simple framework, the net effect of the presence of a nearby QSO would be to *reduce* the column densities of Lyman  $\alpha$  systems. Since we are working with column-density-limited samples, some of the clouds that would be detectable in the absence of the proximity effect will now get a column density below our thresholds and they will therefore disappear. Now the number of absorption lines (for a fixed  $\omega_Q$ ) above the completeness threshold will decrease by a factor  $(1 + \omega_Q)^{1-\beta}$ . Therefore the redshift distribution given by equation (1) has to be revised by the presence of both the background and the foreground QSO, i.e.,

$$\frac{d\mathcal{N}}{dz} = A(1+z)^\gamma (1+\omega_f)^{1-\beta} (1+\omega_b)^{1-\beta} \quad (6)$$

for each QSO distribution.

Notice that if we adopt the values  $A = 8.5$ ,  $\gamma = 1.987$  and the estimates of the QSO luminosities as discussed above, the only free parameter in this equation is the UV background  $J_0$ . In what follows we shall assume that  $J_0$  does not depend on redshift, given the relatively restricted redshift range spanned by our observations. In fact, models for the origin of the UV background in terms of the integrated QSO emission produce a UV background which does not vary very much in the range under consideration. This is a result of the cancellation of the expansion of the universe by the peak in the redshift distribution of the QSO population (see, e.g., Atwood, Baldwin & Carswell 1985; Bechtold et al. 1987).

Since we are interested in the proximity effect caused by the foreground QSOs, we will ignore the inverse effect portion of the different spectra, i.e., the region where photoionization by the background QSO will affect the distribution of lines. This is only relevant to the spectrum of QSO1222+228 in which we have ignored a range of  $5000 \text{ km s}^{-1}$  around the redshift of the QSO. We checked with our best-fitting values for  $J_0$  that this region was large enough to exclude the inverse effect region of this QSO. This also allows us to ignore the  $(1 + \omega_b)^{1-\beta}$  factor in eq (7).

## 5.2 Estimates of the UV ionizing flux

We have performed a one-parameter maximum-likelihood fit to  $\frac{d\mathcal{N}}{dz}$  to find  $J_0$ . The absence of proximity effect would yield  $J_0 = \infty$ . The value of  $J_0$  that maximizes the likelihood function (see Fig. 4) is  $\log J_0 = -20.5$  in the usual units ( $\text{erg cm}^{-2} \text{ s}^{-1} \text{ Hz}^{-1} \text{ srad}^{-1}$ ).

In principle, this kind of fit should also allow us to estimate the errors in the fitted parameter, by using the likelihood function as a probability in parameter space. However, it appears that the likelihood function is unable to be normalized, because once the UV flux  $J_0$  has gone above some value the fitting is insensitive to it (the foreground QSO no longer influences the Lyman  $\alpha$  forest) and the Likelihood function goes to a non-zero constant as  $J_0 \rightarrow \infty$ . Another way to estimate errors from the likelihood function (used, e.g., by Kulkarni & Fall 1993 to estimate the UV background at low  $z$  via the inverse effect) uses the derivatives of the likelihood function around its maximum. However, this is not feasible in our case as the peak that we obtain in the likelihood function is not very pronounced. On the other hand

(see Fig. 4), the Likelihood function presents a strong decay for low values of  $\log(J_0)$ , which would mean the rejection of very low values of  $J_0$  as the proximity effect should be much stronger than observed.

In order to check whether our result is significant (i.e., whether a proximity effect is detected) we have carried out a number of tests. Unfortunately, none of them places our measurement more than  $1\sigma$  away from the inexistence of the proximity effect ( $J_0 = \infty$ ). The most illustrative method is to generate synthetic line lists for the three QSOs in our sample with line densities according to equation (6) and then apply the same method to the simulated lists as to the real data. The result, rather discouraging, is that with the current sample and with  $J_0 = \infty$  there is a probability  $\sim 35$  per cent of measuring a value of  $J_0 < 10^{-20.5} \text{ erg cm}^{-2} \text{ s}^{-1} \text{ Hz}^{-1} \text{ srad}^{-1}$  by chance.

A complementary test has been provided by the use of the bootstrap method, as presented by Efron & Tibshirani (1986). By using 500 bootstrap reshuffled absorption line samples, we have seen that only 15 per cent of them do not show any local maximum in the likelihood function (i.e., only 15 per cent of the bootstrapped samples give  $J_0 = \infty$ ). We can now use this distribution of  $J_0$  values to try to assess error bars to the value that maximizes the likelihood function. The result is that the  $1\sigma$  upper bound just hits the  $J_0 = \infty$  value in complete agreement with the previous method.

We then conclude that although our results are consistent with a proximity effect caused by a UV background of the order of  $J_0 = 10^{-20.5} \text{ erg cm}^{-2} \text{ s}^{-1} \text{ Hz}^{-1} \text{ srad}^{-1}$ , we cannot rule out that the effect is in fact not present. In Figure 5 we show a binned distribution of the Lyman  $\alpha$  absorption lines as a function of  $\log(F_f^2/4\pi)$ —where  $F_f$  is the flux from the foreground QSO, locally normalised to the overall redshift distribution (equation 1). The proximity effect implies a decrease of this function at large values of the foreground QSO flux. We also show the expected distribution for different values of  $J_0$ . This diagram illustrates that although there is some hint that the proximity effect might be present, its detection (i.e., discrimination from the  $J_0 = \infty$  curve) is indeed difficult.

Unfortunately, the closest distance from a foreground QSO to the line of sight of the corresponding background QSO is quite large ( $1.7 h_{50}^{-1} \text{ Mpc}$ ) which does not enable us to explore the diagram presented in Fig. 5 at higher values of  $\log(F_f^2/4\pi)$ . Indeed, this is much better achieved by including the inverse effect caused by the background QSO itself. In fact, and as a test, we have used the whole available spectrum of QSO1222+228, which also contains the inverse effect range. The likelihood function now exhibits a very pronounced peak (see Fig. 6) and the measured UV background is now  $\log J_0 = -21.1 \pm 0.6 \text{ erg cm}^{-2} \text{ s}^{-1} \text{ Hz}^{-1} \text{ srad}^{-1}$ .

We can also use the bootstrap results to find lower bounds to the UV intensity within the photoionization model. These come from the fact that a UV background that is too low would imply an unacceptably large proximity effect. At 95 per cent confidence, the UV ionizing flux is  $J_0 > 10^{-21.8} \text{ erg cm}^{-2} \text{ s}^{-1} \text{ Hz}^{-1} \text{ srad}^{-1}$ . This limit is quite secure because our sample contains a pair (QSO1055+021) that would show some hint of proximity effect if  $J_0$  were low enough, while no evidence is found for it in that particular spectrum. We discuss in next Section the implications of

this lower limit for the origin of the UV background at high redshift.

## 6 DISCUSSION

To our knowledge there are only two previous observational works about the detection of the proximity effect by foreground QSOs (Crotts 1989; Dobrzycki & Bechtold 1991). Crotts(1989) uses spectra of QSO1623+268 and three other QSOs in its neighbourhood. In that work no proximity effect is detected at  $2.4\sigma$  level, and the author suggests that either the QSO radiation is highly anisotropic or that the proximity effect has causes other than radiation. Dobrzycki & Bechtold (1991) find a void at  $z = 3.17$  towards QSO0302-003, which is not coincidental with the redshift of a known foreground QSO ( $z = 3.223$ ). In order to interpret this void in terms of the proximity effect of the foreground QSO, these authors conclude that its radiation has to be highly anisotropic.

Like all of the above authors, we have ignored the fact that there is possibly variability in the QSOs. There are two possible sources for this variability. First, we could be observing some kind of long-term fading in the QSOs. We do not believe this effect to be significant, since pure luminosity evolution models for the QSO population show that the time-scale for this effect is much longer than the light travel time from the QSO to the cloud (typically 30 Myrs). On the other hand, we cannot forget the possibility of having short-scale variability. In any case, it is impossible to model this effect, as there is only statistical information on this phenomenon. Moreover we can expect this effect to be less important when a larger sample is used (because of cancellation of individual changes). Hence, we believe that to neglect variability is our best choice. It is worth mentioning that this problem is not present in the measurements of  $J_\nu$  when the proximity effect of the QSO on its own line of sight is used.

We think that the set of statistical tools used in our work to search for the proximity effect is quite appropriate. The use of simulations of both the line lists and the bootstrap technique to assess significance levels and confidence intervals are in very good agreement. Taking the Likelihood function for the redshift distribution of the lines as the statistic to be maximized in the fitting procedure, we do not require to bin the data, which is very important when only a limited amount of data are available. A *log likelihood* analysis [as used, e.g., by Shafer (1983) in a different context] also gave similar results. This method also showed that the sample should be much increased (by a factor of at least 10 in the number of lines) in order to be able to exclude  $J_0 = \infty$  at, say, 95 per cent confidence.

We have also made other attempts to detect the proximity effect, with similar success. For example, comparing the summed column density in a window of  $\pm 5000 \text{ km s}^{-1}$  around the known redshift of the foreground QSO with the same value for a set of simulations generated with different trial values of  $J_0$ , also shows a best fit for  $J_0 \sim 10^{-20.5} \text{ erg cm}^{-2} \text{ s}^{-1} \text{ Hz}^{-1} \text{ srad}^{-1}$ ; but again, when we try to estimate the error bar for that value, we find that  $J_0 = \infty$  (i.e., no proximity effect) is only about  $1\sigma$  away.

Comparing our results with the available UV background flux models (basically Bechtold et al. 1987 which

are also used by BDO), we can reach some conclusions. We have selected the models presented in that paper with  $q_0 = 0.5$ , including absorption from Lyman  $\alpha$  clouds, diffuse neutral hydrogen and thick Lyman  $\alpha$  absorbers. In that work, the UV background contributed by QSOs is estimated at different redshifts by assuming different QSO evolution models. Since our study is aimed at testing this quantity in the range  $z \sim 1.7 - 2.7$ , where most QSOs have been switched on, we cannot distinguish between models with different types of redshift cut-offs. The final result of these models is that the UV ionizing flux at the redshifts under consideration lies between  $10^{-21.8} \text{ erg cm}^{-2} \text{ s}^{-1} \text{ Hz}^{-1} \text{ srad}^{-1}$  and  $10^{-22} \text{ erg cm}^{-2} \text{ s}^{-1} \text{ Hz}^{-1} \text{ srad}^{-1}$ , i.e. below our  $2\sigma$  lower limit. Similar results are obtained when comparing with models in Madau (1992) and Meiksin & Madau (1993). This means that our work agrees with the suggestion by Bechtold et al. (1987), BDO and others, i.e. that *observed* QSOs do not appear to be either luminous or numerous enough to explain all of the UV background flux that is inferred at intermediate redshift.

One possible alternative is that some kind of absorber (dust?) is obscuring an important part of the light from QSOs between redshift 2 and 0. This would imply that the QSO population at medium to high redshift is larger than the one we observe (see, e.g., models by Heisler & Ostriker 1988). That, however, would imply a systematic reddening of the high redshift QSOs which is not consistent with the low dust content of the thick absorbers (Fall & Pei 1989; Fall, Pei & MacMahon 1990).

Another possibility that could explain the UV excess would be to postulate the presence of a large amount of unobserved high-redshift star-forming galaxies (see e.g. Madau 1991). It is hard to make this thesis compatible with present-day galaxy luminosity functions. In fact, there is much controversy nowadays about the feasibility of the presence of a large number of *dwarf galaxies* with  $22 < M < 27$ , at  $z \simeq 2$  (see, e.g., Cowie, Songaila & Hu 1991; Efstathiou 1992; Cole, Treyer & Silk 1992). None the less, one would expect that high- $z$  star-forming galaxies contain large amounts of dust (as is observed at low redshift), which would preclude any relevant amount of UV photons escaping from these objects.

An explanation for the proximity effect which is also entirely consistent with our data is the one where QSOs reside in the depths of strong gravitational potential wells and Lyman  $\alpha$  clouds fall onto those potential wells. This cleans up the neighbourhood of a  $z = 2.5$  QSO within a radius of  $0.3h_{50}^{-1} \sigma_{100} \text{ Mpc}$  in less than a Hubble time, where  $\sigma_{100}$  is the velocity dispersion in the potential well in units of  $100 \text{ km s}^{-1}$ . If QSOs exist in high-density environments where velocity dispersions are high, it is possible to explain the proximity effect in these terms. In fact, Vishniac & Bust (1987) and Barcons & Webb (1990) discussed similar mechanisms to explain the lack of clustering of Lyman  $\alpha$  clouds around galaxies (represented by heavy-element systems) in biased scenarios for the formation of these objects, where such clustering would be expected.

We believe that the results obtained by Crotts (1989) and Dobrzycki & Bechtold (1991), are not inconsistent with the present work. Using a very simple model for the QSO emission (an opaque torus surrounding the central source as suggested by the AGN unified scheme) and the opening angle  $\sim 140^\circ$  given in Dobrzycki and Bechtold (1991), it turns



out that the case where the system behaves *as if the radiation from the foreground QSO were emitted isotropically* (i.e. when the opacity towards the observer and towards the point of closest approach in the line of sight to the background QSO are similar) has a probability  $\simeq 50$  per cent. It is also expected that in some cases ( $\simeq 25$  per cent according to that naïve model) the torus obscures the direction towards the background QSO line of sight but not the direction towards the observer, and the inverse effect would not be seen. In the remaining  $\simeq 25$  per cent of the cases the torus will obscure the foreground QSO from the observer but would ionize the background QSO line of sight. All these numbers are derived from the estimate by Dobrzycki and Bechtold (1991) of the obscuring angle, which is based in a single case and therefore could change when more information becomes available from other QSO pair observations.

The model for Lyman  $\alpha$  clouds, where these are low-density highly ionized galaxy-sized gas aggregates, provides the most basic scenario that is consistent with our observations. Although this is the model preferred by the data we cannot, unfortunately, rule out other non-local explanations for the inverse effect. More definite conclusions, especially the ones concerning the isotropy of the emission, could be achieved by means of observing a larger sample of QSO pairs.

### Acknowledgments

AFS thanks Adam Dobrzycki for useful comments on an original version of this paper. AFS and RC acknowledge support by a research grant by the Spanish MEC. Partial financial support for this work was provided by the DGICYT under project PB92-0741 and by the Commission of the European Union under the ‘Human Capital and Mobility’ contract CHRX-CT92-0033. The Isaac Newton Telescope (INT) and the William Herschel Telescope (WHT) are operated on the island of La Palma by the Royal Greenwich Observatory in the Spanish Observatorio del Roque de Los Muchachos of the Instituto de Astrofísica de Canarias. The spectrum of 1305+298 was taken during a service night at WHT.

### REFERENCES

- Atwood, B., Baldwin, J.A., Carswell, R.F., 1985, ApJ, 292, 58  
 Bahcall, J.N., Osmer, P.S., Schmidt, M., 1969, ApJ, 156, L1  
 Bajtlik, S., Duncan, R.C., Ostriker, J.P., 1988, ApJ, 327, 570 (BDO)  
 Barcons, X., Webb, J.K., 1990, MNRAS, 244, 30p  
 Barcons, X., Fabian, A.C., 1987, MNRAS, 229, 157  
 Bechtold, J., Green, R.F., Weymann, R.J., Schmidt, M., Estabrook, F.B., Sherman, R.D., Wahlquist, H.D., Heckman, T.M., 1984, ApJ, 281, 76  
 Bechtold, J., Weymann, R.J., Lin, Z., Malkon, M.A., 1987, ApJ, 315, 180  
 Bechtold, J., Crotts, A.P.S., Duncan, R.C., Fang, Y., 1994, ApJ, 437, L83  
 Bechtold, J., 1994, ApJS, 91, 1  
 Carswell, R.F., Webb, J.K., Baldwin, J.A., Atwood, B., 1987, ApJ, 319, 709  
 Carswell, R.F., Whelan, J.A.J., Smith, M.G., Bokkenberg, A., Tytler, D., 1982, MNRAS, 198, 91  
 Cole, S., Treyer, M.A., Silk, J., ApJ, 1992, 385, 9  
 Cowie, L.L., Songaila, A., Hu, E.M. 1991, Nat, 354, 460

- Crotts, A.P.S., 1989, ApJ, 336, 550  
 Dinshaw, N., Impey, C.D., Foltz, C.B., Weymann, R.J., Chaffee, F.H., 1994, ApJ, 437, L87  
 Dobrzycki, A., Bechtold, J., 1991, ApJ, 377, L69  
 Efron, B., Tibshirani, R., 1986, Stat. Sci., 1, 54  
 Efstathiou, G. 1992, MNRAS, 256, 43p  
 Evans, A., Hart, D., 1977, A&A, 58, 241  
 Fall, S.M., Pei, Y.C., 1989, ApJ, 267, 535  
 Fall, S.M., Pei, Y.C., McMahon, R.G. 1990, ApJ, 341, L5  
 Heisler, J., Ostriker, J.P., 1988, ApJ, 325, 103  
 Hewitt, A., Burbidge, G., 1993, ApJS, 87, 451  
 Hippelein, H., Meisenheimer, K., 1993, Nat, 362, 224  
 Kulkarni, V.P., Fall, S.M., 1993, ApJ, 413, L63  
 Lu, L., Wolfe, A.M., Turnshek, D.A., 1991, ApJ, 367, 19  
 Madau, P., 1991, ApJ, 376, L33  
 Madau, P., 1992, ApJ, 389, L1  
 Meiksin, A., Madau, P., 1993, ApJ, 412, 34  
 Morton, W.A., Morton, D.C., 1972, ApJ, 178, 607  
 Murdoch, H.S., Hunstead, R.W., Pettini, M., Blades, J.C., 1986, ApJ, 309, 19  
 Robertson, J.G., Shaver, P.A., 1983, MNRAS, 204, 69p  
 Sargent, W.L.W., Bokkenberg, A., Steidel, C., 1988, ApJS, 68, 539  
 Shafer, R.A., 1983, PhD Thesis, Univ. of Maryland  
 Smette, A., Surdej, J., Shaver, P.A., Foltz, C.B., Chaffee, F.H., Weymann, R.J., Williams, R.E., Magan, P., 1992, ApJ, 389, 39  
 Tytler, D.A., 1987, ApJ, 321, 69  
 Vishniac, E.T., Bust, G.S., 1987, ApJ, 319, 14  
 Webb, J.K., Larsen, I., 1988, in Bergeron, J., Knuth, D., Rocca-Volmerange, B., eds, High z and Primeval Galaxies, Editions Frontières, Gif-sur-Yvette  
 Webb, J.K., Barcons, X., Carswell, R.F., Parnell, H.C., 1992, MNRAS, 255, 319  
 Weymann, R.J., Carswell, R.F., Smith, M.G., 1981, ARA&A, 19, 41  
 Young, P.J., Sargent, W.L.W., Bokkenberg, A., Carswell, R.F., Whelan, J.A.J., 1979, ApJ, 229, 891

This paper has been produced using the Royal Astronomical Society/Blackwell Science L<sup>A</sup>T<sub>E</sub>X style file.

**FIGURE CAPTIONS**

Figure 1: The spectrum of QSO 1055+021. See text for details.

Figure 2: The spectrum of QSO 1222+228. See text for details.

Figure 3: The spectrum of QSO 1228+077. See text for details.

Figure 4: Likelihood function in terms of  $\log J_0$ . The inverse effect region in QSO1222+228 has been excluded.

Figure 5: Normalised Lyman  $\alpha$  absorption line density (after removal of the overall trend with  $z$ ) as a function of the flux from the foreground QSO.

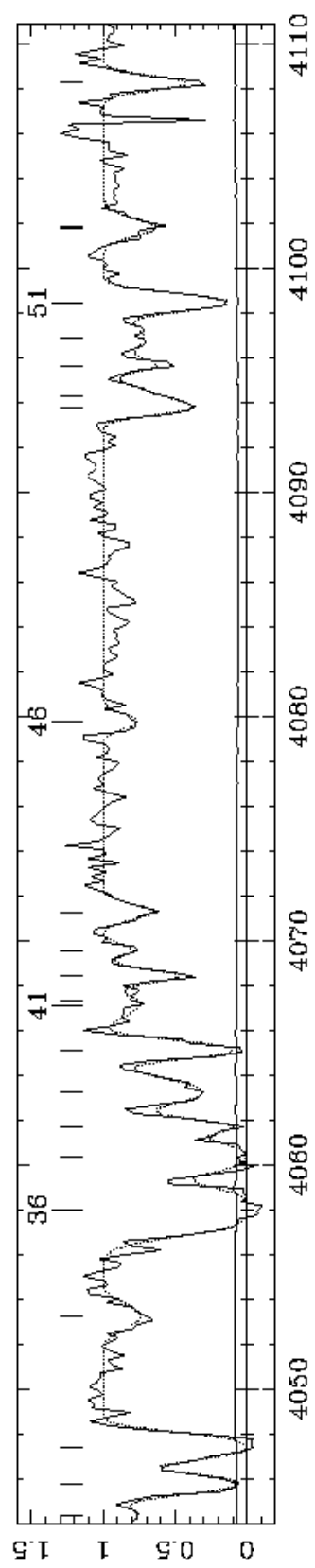
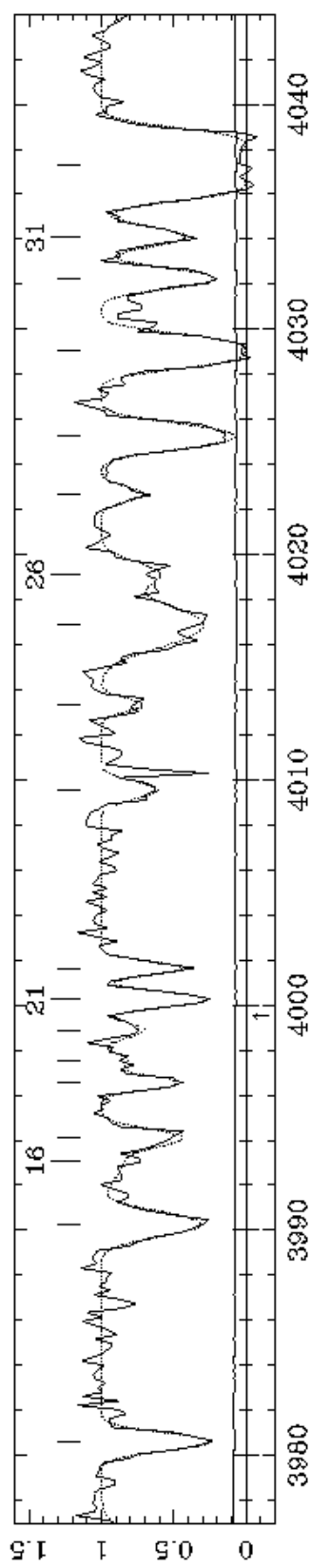
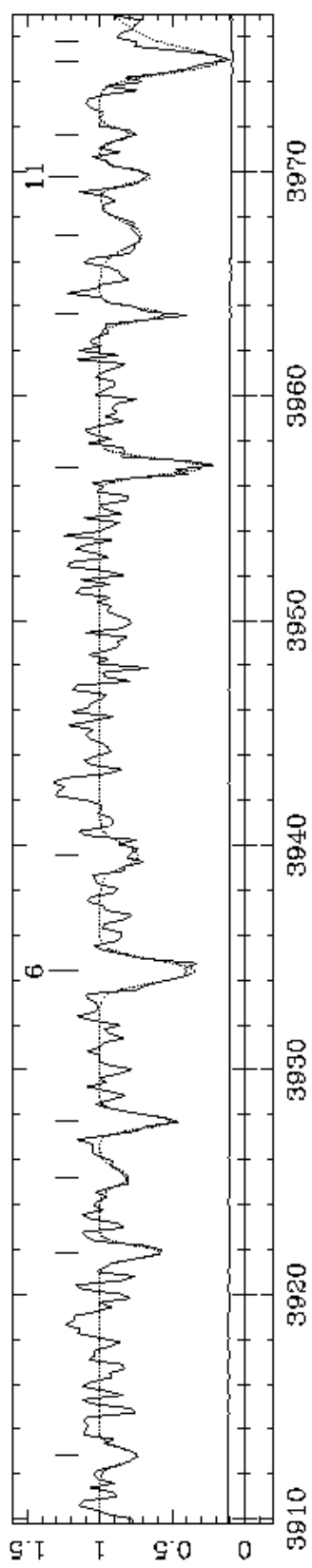
Figure 6: Likelihood function in terms of  $\log J_0$ . The inverse effect region in QSO1222+228 has not been excluded.

**TABLE CAPTIONS**

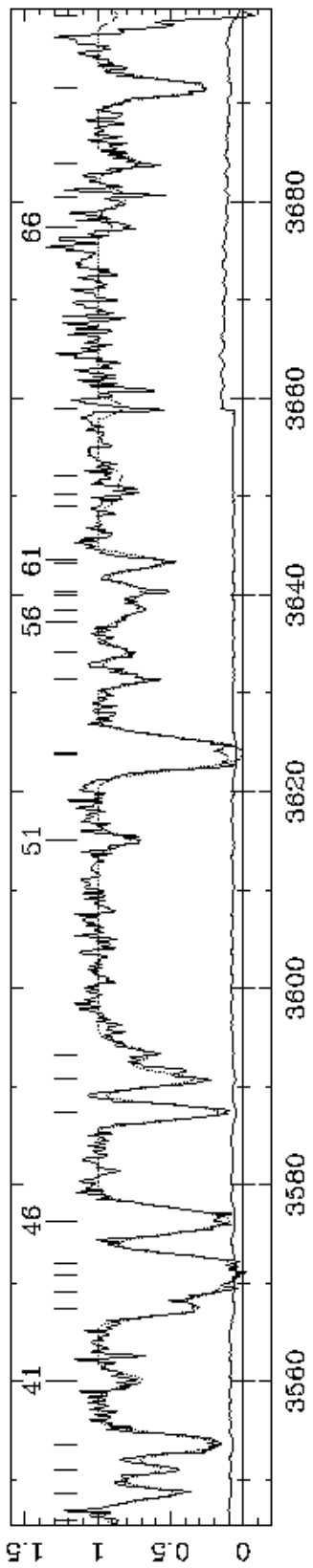
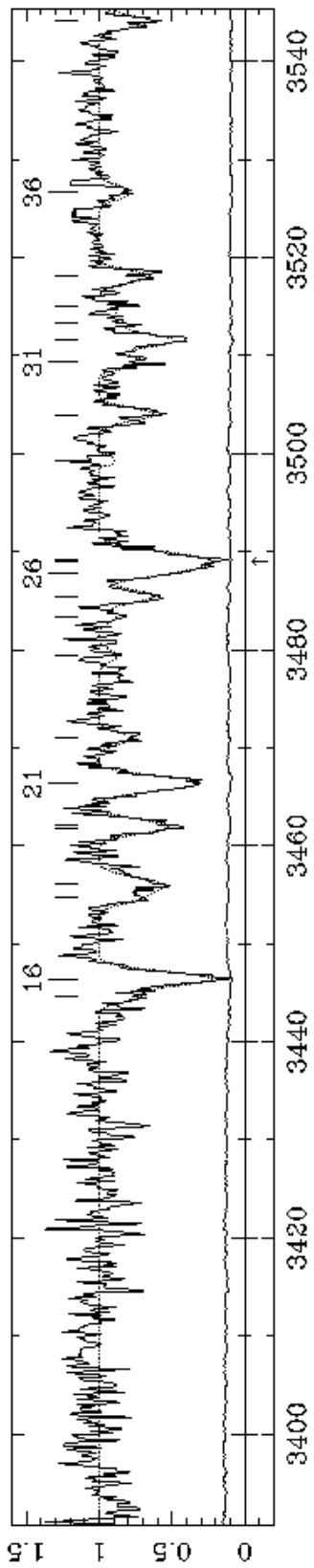
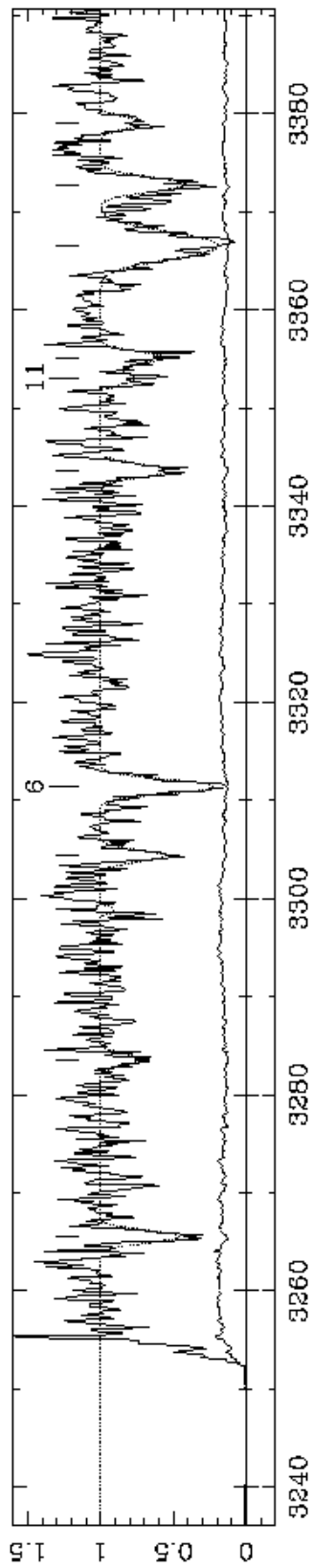
Table 3: QSO 1055+021: absorption lines list. See text for details.

Table 4: QSO 1222+228: absorption lines list. See text for details.

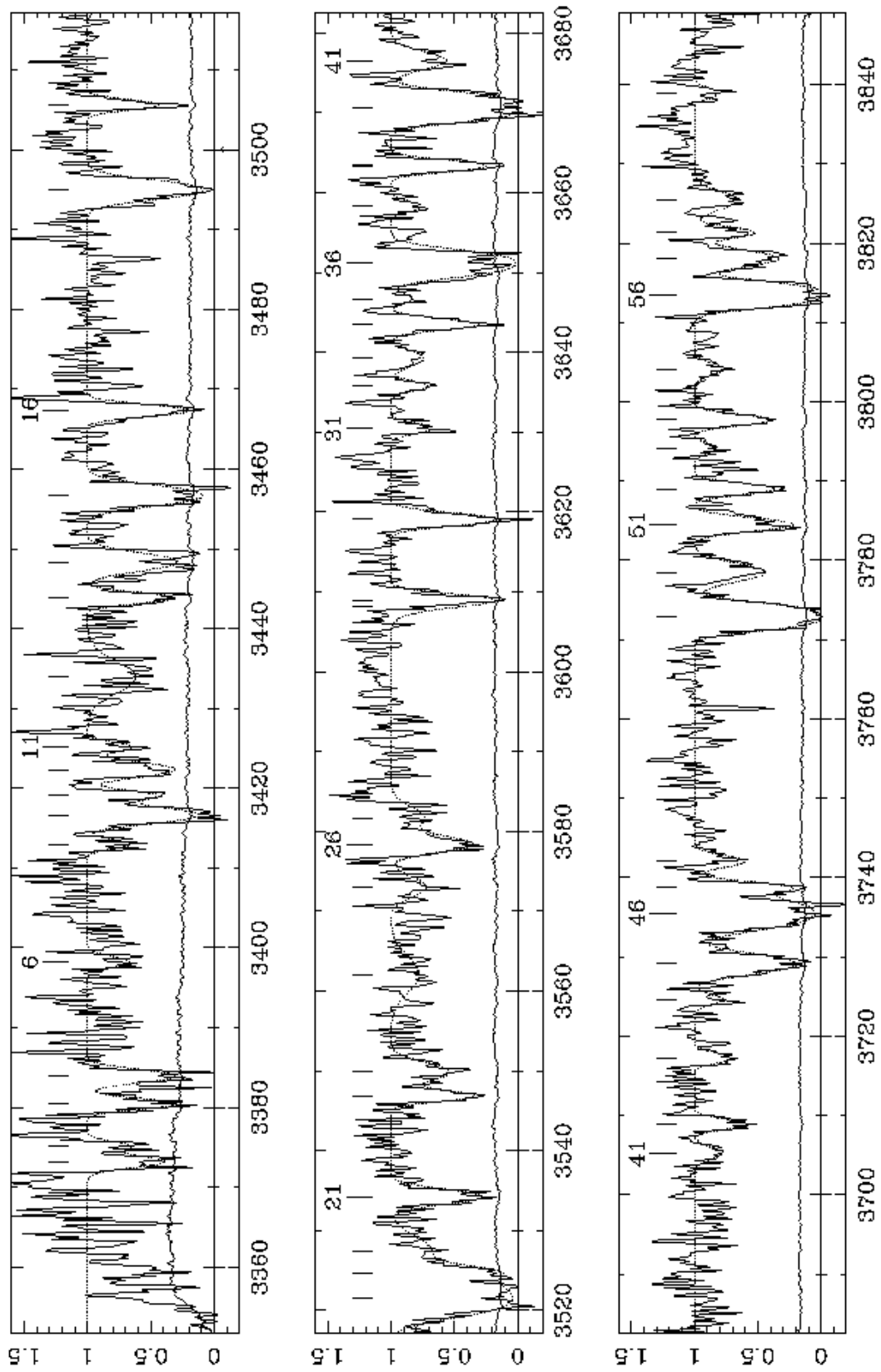
Table 5: QSO 1228+077: absorption lines list. See text for details.



Wavelength (Angstroms)



Wavelength (Angstroms)



Wavelength (Angstroms)

**Table 3.** QSO 1055+021 : Absorption lines list. See text for details.

$N^\circ$	$\lambda_{obs}$	Ident.	$z$	$10^6 \Delta z$	$N$	$\Delta N$	$b$	$\Delta b$	SYST.	
1	3912.9	Ly $\alpha$	1216	2.218644	90	$1.4 \cdot 10^{13}$	$4.3 \cdot 10^{12}$	20	20	
2	3921.9	Ly $\alpha$	1216	2.226103	49	$3.2 \cdot 10^{13}$	$4.6 \cdot 10^{13}$	11	17	
3	3925.2	Ly $\alpha$	1216	2.228851	124	$1.1 \cdot 10^{13}$	$4.1 \cdot 10^{12}$	28	22	
4	3927.7	Ly $\alpha$	1216	2.230896	41	$4.0 \cdot 10^{13}$	$2.6 \cdot 10^{13}$	14	11	
5	3934.4	Ly $\alpha$	1216	2.236394	40	$6.8 \cdot 10^{13}$	$8.6 \cdot 10^{12}$	37	6	
6	3939.5	Ly $\alpha$	1216	2.240639	104	$2.1 \cdot 10^{13}$	$5.0 \cdot 10^{12}$	44	16	
7	3956.8	Ly $\alpha$	1216	2.254867	30	$9.2 \cdot 10^{13}$	$7.4 \cdot 10^{13}$	18	8	
8	3963.6	SiII	1260	2.144685	43	$1.3 \cdot 10^{13}$	$1.0 \cdot 10^{13}$	12	13	1
9	3967.1	Ly $\alpha$	1216	2.263326	95	$2.7 \cdot 10^{13}$	$5.0 \cdot 10^{12}$	53	14	
10	3969.8	Ly $\alpha$	1216	2.265503	52	$2.1 \cdot 10^{13}$	$7.5 \cdot 10^{12}$	14	14	
11	3971.6	Ly $\alpha$	1216	2.267035	85	$1.1 \cdot 10^{13}$	$2.6 \cdot 10^{13}$	7	40	
12	3974.9	Ly $\alpha$	1216	2.269740	28	$1.1 \cdot 10^{14}$	$1.3 \cdot 10^{13}$	37	4	
13	3975.8	AlIII	1854	1.143596	104	$1.8 \cdot 10^{13}$	$4.0 \cdot 10^{12}$	78	20	3
14	3980.6	Ly $\alpha$	1216	2.274413	25	$8.4 \cdot 10^{13}$	$1.8 \cdot 10^{13}$	24	5	
15	3990.3	Ly $\alpha$	1216	2.282368	29	$8.0 \cdot 10^{13}$	$6.7 \cdot 10^{12}$	43	4	
16	3993.1	AlIII	1862	1.143596	104	$1.8 \cdot 10^{13}$	$4.0 \cdot 10^{12}$	78	20	3
17	3994.1	Ly $\alpha$	1216	2.285516	34	$4.2 \cdot 10^{13}$	$4.7 \cdot 10^{12}$	27	6	
18	3996.6	Ly $\alpha$	1216	2.287529	29	$8.0 \cdot 10^{14}$	$4.6 \cdot 10^{16}$	7	43	
19	3997.5	Ly $\alpha$	1216	2.288324	95	$9.0 \cdot 10^{12}$	$2.9 \cdot 10^{12}$	15	28	
20	3998.9	Ly $\alpha$	1216	2.289437	57	$1.7 \cdot 10^{13}$	$2.9 \cdot 10^{12}$	21	14	
21	4000.2	Ly $\alpha$	1216	2.290563	20	$2.0 \cdot 10^{14}$	$7.4 \cdot 10^{14}$	13	11	
22	4001.6	Ly $\alpha$	1216	2.291715	55	$1.2 \cdot 10^{15}$	$5.5 \cdot 10^{16}$	7	35	
23	4009.5	Ly $\alpha$	1216	2.298213	42	$2.7 \cdot 10^{13}$	$3.4 \cdot 10^{12}$	27	8	
24	4013.3	Ly $\alpha$	1216	2.301331	49	$1.6 \cdot 10^{13}$	$3.9 \cdot 10^{12}$	14	13	
25	4016.9	SiIII	1206	2.329327	37	$3.4 \cdot 10^{13}$	$1.9 \cdot 10^{12}$	78	5	2
26	4019.1	Ly $\alpha$	1216	2.306094	67	$3.7 \cdot 10^{13}$	$5.2 \cdot 10^{12}$	48	9	
27	4022.7	Ly $\alpha$	1216	2.309022	51	$1.6 \cdot 10^{13}$	$2.8 \cdot 10^{12}$	19	11	
28	4025.3	Ly $\alpha$	1216	2.311138	19	$1.7 \cdot 10^{14}$	$3.3 \cdot 10^{13}$	35	3	
29	4029.0	Ly $\alpha$	1216	2.314249	25	$6.5 \cdot 10^{14}$	$7.4 \cdot 10^{14}$	34	9	
30	4032.3	Ly $\alpha$	1216	2.316903	21	$9.6 \cdot 10^{13}$	$1.5 \cdot 10^{13}$	28	4	
31	4034.1	Ly $\alpha$	1216	2.318425	29	$5.1 \cdot 10^{13}$	$5.0 \cdot 10^{12}$	31	5	
32	4037.3	Ly $\alpha$	1216	2.321069	19	$9.9 \cdot 10^{15}$	$1.4 \cdot 10^{16}$	53	8	
33	4044.3	Ly $\alpha$	1216	2.326821	98	$1.8 \cdot 10^{13}$	$4.0 \cdot 10^{12}$	42	16	
34	4045.8	Ly $\alpha$	1216	2.328017	20	$4.6 \cdot 10^{14}$	$1.2 \cdot 10^{15}$	21	11	
35	4047.4	Ly $\alpha$	1216	2.329357	21	$2.9 \cdot 10^{15}$	$1.9 \cdot 10^{16}$	22	17	2
36	4053.2	AlI	3083	0.314686	23	$2.0 \cdot 10^{13}$	$2.4 \cdot 10^{12}$	45	9	4
37	4058.0	Ly $\alpha$	1216	2.338085	32	$5.9 \cdot 10^{14}$	$2.2 \cdot 10^{14}$	59	7	
38	4060.4	Ly $\alpha$	1216	2.340016	32	$4.0 \cdot 10^{14}$	$2.5 \cdot 10^{14}$	43	10	
39	4061.7	Ly $\alpha$	1216	2.341119	29	$1.1 \cdot 10^{16}$	$4.3 \cdot 10^{17}$	11	38	
40	4063.3	Ly $\alpha$	1216	2.342396	33	$8.8 \cdot 10^{13}$	$6.8 \cdot 10^{12}$	49	5	
41	4065.1	Ly $\alpha$	1216	2.343944	20	$3.2 \cdot 10^{15}$	$5.9 \cdot 10^{16}$	14	26	
42	4067.1	AlI	3093	0.314686	23	$2.0 \cdot 10^{13}$	$2.4 \cdot 10^{12}$	45	9	4
43	4067.3	AlI	3093	0.314686	23	$2.0 \cdot 10^{13}$	$2.4 \cdot 10^{12}$	45	9	4
44	4068.4	Ly $\alpha$	1216	2.346651	35	$5.2 \cdot 10^{13}$	$8.5 \cdot 10^{13}$	12	13	
45	4069.6	Ly $\alpha$	1216	2.347608	67	$1.5 \cdot 10^{13}$	$1.3 \cdot 10^{14}$	5	48	
46	4071.3	Ly $\alpha$	1216	2.349013	44	$2.1 \cdot 10^{13}$	$3.2 \cdot 10^{12}$	20	9	
47	4079.8	Ly $\alpha$	1216	2.356007	59	$1.3 \cdot 10^{13}$	$2.4 \cdot 10^{12}$	20	13	
48	4093.8	Ly $\alpha$	1216	2.367512	100	$7.1 \cdot 10^{13}$	$2.9 \cdot 10^{14}$	11	34	
49	4094.3	Ly $\alpha$	1216	2.367964	596	$2.5 \cdot 10^{13}$	$4.3 \cdot 10^{13}$	34	55	
50	4095.7	Ly $\alpha$	1216	2.369074	43	$4.5 \cdot 10^{13}$	$6.6 \cdot 10^{14}$	6	29	

Table 3. Continued.

$N^\circ$	$\lambda_{obs}$	Ident.	$z$	$10^6 \Delta z$	N	$\Delta N$	$b$	$\Delta b$	SYST.	
51	4096.9	Ly $\alpha$	1216	2.370080	137	$3.1 \cdot 10^{13}$	$8.2 \cdot 10^{12}$	65	26	
52	4098.5	Ly $\alpha$	1216	2.371389	19	$2.8 \cdot 10^{14}$	$6.8 \cdot 10^{14}$	18	10	
53	4101.8	SiII	1304	2.144685	43	$1.3 \cdot 10^{13}$	$1.0 \cdot 10^{13}$	12	13	1
54	4101.9	Ly $\alpha$	1216	2.374157	70	$2.0 \cdot 10^{13}$	$4.7 \cdot 10^{12}$	34	12	
55	4108.3	Ly $\alpha$	1216	2.379449	29	$5.6 \cdot 10^{13}$	$4.1 \cdot 10^{13}$	14	8	

Table 4. QSO 1222+228 : Absorption lines list. See Table 3 for details.

$N^\circ$	$\lambda_{obs}$	Ident.	$z$	$10^6 \Delta z$	N	$\Delta N$	$b$	$\Delta b$	SYST.	
1	3265.5	Ly $\alpha$	1216	1.686193	85	$1.5 \cdot 10^{14}$	$3.7 \cdot 10^{14}$	29	41	
2	3283.6	Ly $\alpha$	1216	1.701043	153	$4.1 \cdot 10^{13}$	$8.9 \cdot 10^{13}$	23	97	
3	3298.8	Fe II	2344	0.407228	103	$2.0 \cdot 10^{13}$	$6.2 \cdot 10^{12}$	43	64	6
4	3304.3	Ly $\alpha$	1216	1.718126	123	$9.8 \cdot 10^{13}$	$4.6 \cdot 10^{14}$	25	88	
5	3311.4	Ly $\alpha$	1216	1.723939	54	$2.2 \cdot 10^{15}$	$4.1 \cdot 10^{16}$	28	66	
6	3331.7	Fe II	2260	0.473718	28	$6.6 \cdot 10^{13}$	$1.3 \cdot 10^{13}$	39	13	5
7	3331.7	Fe II	2367	0.407228	103	$2.0 \cdot 10^{13}$	$6.2 \cdot 10^{12}$	43	64	6
8	3341.4	Fe II	2374	0.407228	103	$2.0 \cdot 10^{13}$	$6.2 \cdot 10^{12}$	43	64	6
9	3343.6	Ly $\alpha$	1216	1.750428	92	$8.7 \cdot 10^{13}$	$5.1 \cdot 10^{13}$	37	34	
10	3353.1	Fe II	2382	0.407228	103	$2.0 \cdot 10^{13}$	$6.2 \cdot 10^{12}$	43	64	6
11	3355.2	C II	1335	1.514112	87	$4.8 \cdot 10^{14}$	$4.9 \cdot 10^{15}$	20	76	4
12	3366.5	Ly $\alpha$	1216	1.769295	69	$3.1 \cdot 10^{14}$	$2.9 \cdot 10^{13}$	124	12	
13	3372.8	Ly $\alpha$	1216	1.774435	104	$1.2 \cdot 10^{14}$	$3.6 \cdot 10^{13}$	50	29	
14	3379.1	Ly $\alpha$	1216	1.779599	136	$5.6 \cdot 10^{13}$	$2.5 \cdot 10^{14}$	18	81	
15	3444.6	Ly $\alpha$	1216	1.833502	148	$6.2 \cdot 10^{13}$	$1.5 \cdot 10^{15}$	13	181	
16	3446.4	Ly $\alpha$	1216	1.834990	41	$4.1 \cdot 10^{14}$	$7.6 \cdot 10^{14}$	39	21	
17	3454.7	Fe II	2344	0.473718	28	$6.6 \cdot 10^{13}$	$1.3 \cdot 10^{13}$	39	13	5
18	3456.1	C IV	1548	1.232327	65	$1.2 \cdot 10^{14}$	$2.1 \cdot 10^{13}$	49	23	2
19	3461.8	C IV	1551	1.232327	65	$1.2 \cdot 10^{14}$	$2.1 \cdot 10^{13}$	49	23	2
20	3462.1	Mg II	2796	0.238072	39	$2.5 \cdot 10^{13}$	$2.1 \cdot 10^{13}$	14	8	7
21	3466.4	Ly $\alpha$	1216	1.851394	45	$2.1 \cdot 10^{14}$	$1.1 \cdot 10^{14}$	43	14	
22	3471.0	Mg II	2803	0.238072	39	$2.5 \cdot 10^{13}$	$2.1 \cdot 10^{13}$	14	8	7
23	3479.4	Si II	1190	1.922814	107	$2.5 \cdot 10^{13}$	$1.2 \cdot 10^{14}$	17	61	10
24	3483.3	C I	1560	1.232440	265	$9.2 \cdot 10^{13}$	$1.2 \cdot 10^{16}$	6	607	2
25	3485.4	Ly $\alpha$	1216	1.867092	83	$7.0 \cdot 10^{13}$	$9.3 \cdot 10^{13}$	25	38	
26	3487.8	Si II	1193	1.922814	107	$2.5 \cdot 10^{13}$	$1.2 \cdot 10^{14}$	17	61	10
27	3489.0	Ly $\alpha$	1216	1.869991	50	$2.3 \cdot 10^{14}$	$3.0 \cdot 10^{13}$	73	9	
28	3489.2	Fe II	2367	0.473718	28	$6.6 \cdot 10^{13}$	$1.3 \cdot 10^{13}$	39	13	5
29	3499.3	Fe II	2374	0.473718	28	$6.6 \cdot 10^{13}$	$1.3 \cdot 10^{13}$	39	13	5
30	3504.0	Si IV	1394	1.514053	71	$4.0 \cdot 10^{13}$	$1.1 \cdot 10^{13}$	37	26	4
31	3509.4	Ly $\alpha$	1216	1.886772	109	$5.8 \cdot 10^{13}$	$2.5 \cdot 10^{14}$	19	83	
32	3511.5	Fe II	2382	0.473718	28	$6.6 \cdot 10^{13}$	$1.3 \cdot 10^{13}$	39	13	5
33	3513.4	Ly $\alpha$	1216	1.890080	194	$2.5 \cdot 10^{13}$	$2.8 \cdot 10^{14}$	11	159	
34	3515.0	Ly $\alpha$	1216	1.891398	378	$1.5 \cdot 10^{13}$	$3.5 \cdot 10^{13}$	19	287	
35	3518.1	Ly $\alpha$	1216	1.893935	80	$7.1 \cdot 10^{13}$	$2.1 \cdot 10^{14}$	20	51	
36	3526.6	Si IV	1403	1.514053	71	$4.0 \cdot 10^{13}$	$1.1 \cdot 10^{13}$	37	26	4
37	3544.1	Si III	1206	1.937460	126	$1.3 \cdot 10^{13}$	$6.0 \cdot 10^{12}$	32	44	1 B
38	3545.9	Si III	1206	1.938959	642	$1.9 \cdot 10^{12}$	$5.4 \cdot 10^{12}$	17	494	1 C
39	3548.6	Ly $\alpha$	1216	1.919049	49	$1.7 \cdot 10^{14}$	$3.7 \cdot 10^{14}$	27	25	
40	3551.0	Mg II	2796	0.269866	23	$2.8 \cdot 10^{13}$	$8.8 \cdot 10^{12}$	26	9	8

Table 4. Continued.

$N^{\circ}$	$\lambda_{obs}$	Ident.	$z$	$10^6 \Delta z$	N	$\Delta N$	$b$	$\Delta b$	SYST.	
41	3553.6	Ly $\alpha$	1216	1.923148	35	$3.2 \cdot 10^{14}$	$7.3 \cdot 10^{13}$	63	9	10
42	3560.1	Mg II	2803	0.269866	23	$2.8 \cdot 10^{13}$	$8.8 \cdot 10^{12}$	26	9	8
43	3567.4	Ly $\alpha$	1216	1.934516	44	$2.0 \cdot 10^{14}$	$1.1 \cdot 10^{14}$	41	15	
44	3569.2	Ly $\alpha$	1216	1.935969	172	$2.1 \cdot 10^{14}$	$1.3 \cdot 10^{14}$	49	29	1 A
45	3570.7	Ly $\alpha$	1216	1.937245	156	$6.9 \cdot 10^{14}$	$1.6 \cdot 10^{15}$	66	65	1 B
46	3572.0	Ly $\alpha$	1216	1.938286	151	$3.3 \cdot 10^{14}$	$2.5 \cdot 10^{14}$	17	59	1 C
47	3576.3	Ly $\alpha$	1216	1.941860	29	$4.0 \cdot 10^{14}$	$3.9 \cdot 10^{13}$	89	6	
48	3587.3	Ly $\alpha$	1216	1.950882	671	$5.6 \cdot 10^{14}$	$3.0 \cdot 10^{16}$	22	205	
49	3587.4	Ly $\alpha$	1216	1.950946	655	$4.5 \cdot 10^{14}$	$2.0 \cdot 10^{16}$	24	209	
50	3590.7	Fe II	1608	1.232411	62	$1.0 \cdot 10^{15}$	$9.5 \cdot 10^{14}$	38	24	2
51	3593.2	Ly $\alpha$	1216	1.955743	104	$5.9 \cdot 10^{13}$	$6.6 \cdot 10^{12}$	72	21	
52	3615.0	Si II	1190	2.036761	87	$1.0 \cdot 10^{14}$	$1.5 \cdot 10^{15}$	11	71	3
53	3623.9	Ly $\alpha$	1216	1.980951	23	$1.2 \cdot 10^{15}$	$5.0 \cdot 10^{14}$	87	9	
54	3623.7	Si II	1193	2.036761	87	$1.0 \cdot 10^{14}$	$1.5 \cdot 10^{15}$	11	71	3
55	3631.4	Ly $\alpha$	1216	1.987178	68	$8.5 \cdot 10^{13}$	$4.0 \cdot 10^{14}$	16	38	
56	3634.2	Mg II	2796	0.299617	44	$1.3 \cdot 10^{13}$	$1.1 \cdot 10^{14}$	11	75	9
57	3637.3	N V	1239	1.936153	180	$2.6 \cdot 10^{13}$	$3.5 \cdot 10^{13}$	9	45	1 A
58	3638.5	N V	1239	1.937114	71	$1.1 \cdot 10^{14}$	$3.5 \cdot 10^{13}$	23	22	1 B
59	3640.0	Fe II	2587	0.407228	103	$2.0 \cdot 10^{13}$	$6.2 \cdot 10^{12}$	43	64	6
60	3640.3	N V	1239	1.938583	56	$1.1 \cdot 10^{14}$	$1.1 \cdot 10^{13}$	51	21	1 C
61	3643.2	Ly $\alpha$	1216	1.996848	78	$2.8 \cdot 10^{14}$	$1.1 \cdot 10^{16}$	15	113	
62	3643.5	Mg II	2803	0.299617	44	$1.3 \cdot 10^{13}$	$1.1 \cdot 10^{14}$	11	75	9
63	3649.0	N V	1243	1.936153	180	$2.6 \cdot 10^{13}$	$3.5 \cdot 10^{13}$	9	45	1 A
64	3650.2	N V	1243	1.937114	71	$1.1 \cdot 10^{14}$	$3.5 \cdot 10^{13}$	23	22	1 B
65	3652.1	N V	1243	1.938583	56	$1.1 \cdot 10^{14}$	$1.1 \cdot 10^{13}$	51	21	1 C
66	3659.0	Fe II	2600	0.407228	103	$2.0 \cdot 10^{13}$	$6.2 \cdot 10^{12}$	43	64	6
67	3677.4	Ly $\alpha$	1216	2.024991	426	$1.1 \cdot 10^{13}$	$2.3 \cdot 10^{13}$	19	316	
68	3680.4	Ly $\alpha$	1216	2.027480	294	$2.7 \cdot 10^{13}$	$9.8 \cdot 10^{12}$	54	81	
69	3684.0	Si II	1260	1.922814	107	$2.5 \cdot 10^{13}$	$1.2 \cdot 10^{14}$	17	62	10
70	3691.6	Ly $\alpha$	1216	2.036660	44	$2.1 \cdot 10^{14}$	$4.6 \cdot 10^{13}$	55	9	3
71	3699.0	C I	1656	1.232440	265	$9.2 \cdot 10^{13}$	$1.2 \cdot 10^{16}$	6	607	2

Table 5. QSO 1228+077 : Absorption lines list. See Table 3 for details.

$N^{\circ}$	$\lambda_{obs}$	Ident.	$z$	$10^6 \Delta z$	N	$\Delta N$	$b$	$\Delta b$	SYST.	
1	3373.2	Ly $\beta$	1026	2.288641	281	$7.9 \cdot 10^{14}$	$4.4 \cdot 10^{14}$	55	59	
2	3375.2	Ly $\alpha$	1216	1.776398	307	$7.5 \cdot 10^{13}$	$1.5 \cdot 10^{15}$	18	234	
3	3380.5	Ly $\alpha$	1216	1.780735	130	$3.4 \cdot 10^{14}$	$2.8 \cdot 10^{15}$	32	76	
4	3383.9	Ly $\beta$	1026	2.299082	193	$1.0 \cdot 10^{15}$	$4.0 \cdot 10^{14}$	64	37	4
5	3398.2	Ly $\alpha$	1216	1.795354	267	$4.7 \cdot 10^{13}$	$2.1 \cdot 10^{13}$	48	74	
6	3413.0	Ly $\alpha$	1216	1.807504	220	$7.1 \cdot 10^{13}$	$8.1 \cdot 10^{14}$	17	135	
7	3416.7	C IV	1548	1.206871	68	$5.8 \cdot 10^{14}$	$1.2 \cdot 10^{14}$	77	15	5
8	3419.1	C II	1036	2.299198	157	$2.8 \cdot 10^{15}$	$2.0 \cdot 10^{17}$	19	212	4
9	3422.3	C IV	1551	1.206871	68	$5.8 \cdot 10^{14}$	$1.2 \cdot 10^{14}$	77	15	5
10	3425.2	Ly $\alpha$	1216	1.817517	191	$7.4 \cdot 10^{13}$	$6.1 \cdot 10^{14}$	19	119	
11	3433.9	Ly $\alpha$	1216	1.824705	329	$1.5 \cdot 10^{14}$	$2.7 \cdot 10^{13}$	220	50	
12	3443.8	Ly $\alpha$	1216	1.832871	98	$3.9 \cdot 10^{14}$	$3.5 \cdot 10^{15}$	30	67	
13	3448.4	Si II	1190	1.896765	47	$3.4 \cdot 10^{14}$	$2.9 \cdot 10^{13}$	99	6	1
14	3456.7	Si II	1193	1.896765	47	$3.4 \cdot 10^{14}$	$2.9 \cdot 10^{13}$	99	6	1



Table 5. Continued.

$N^{\circ}$	$\lambda_{obs}$	Ident.	$z$	$10^6 \Delta z$	N	$\Delta N$	$b$	$\Delta b$	SYST.	
15	3467.8	Ly $\alpha$	1216	1.852181	79	$2.5 \cdot 10^{15}$	$6.5 \cdot 10^{16}$	29	95	
16	3495.0	Si III	1206	1.896755	77	$1.0 \cdot 10^{14}$	$2.6 \cdot 10^{13}$	90	14	1
17	3505.6	Ly $\alpha$	1216	1.883688	102	$2.4 \cdot 10^{14}$	$1.7 \cdot 10^{15}$	24	53	
18	3521.6	Ly $\alpha$	1216	1.896851	149	$7.9 \cdot 10^{14}$	$1.3 \cdot 10^{14}$	173	22	1
19	3524.6	Ly $\alpha$	1216	1.899275	179	$2.5 \cdot 10^{14}$	$8.2 \cdot 10^{13}$	74	41	
20	3527.4	Ly $\alpha$	1216	1.901601	604	$1.1 \cdot 10^{14}$	$4.0 \cdot 10^{13}$	198	93	
21	3534.2	Ly $\alpha$	1216	1.907227	87	$1.8 \cdot 10^{14}$	$3.1 \cdot 10^{13}$	74	16	
22	3546.9	Ly $\alpha$	1216	1.917623	86	$4.3 \cdot 10^{14}$	$4.6 \cdot 10^{15}$	27	66	
23	3549.8	Ly $\alpha$	1216	1.920076	178	$1.1 \cdot 10^{14}$	$1.9 \cdot 10^{13}$	114	34	
24	3562.1	Ly $\alpha$	1216	1.930133	908	$8.5 \cdot 10^{13}$	$4.0 \cdot 10^{13}$	251	158	
25	3573.1	Ly $\alpha$	1216	1.939161	296	$6.0 \cdot 10^{13}$	$1.6 \cdot 10^{13}$	125	48	
26	3578.4	Ly $\alpha$	1216	1.943565	106	$1.5 \cdot 10^{14}$	$2.3 \cdot 10^{13}$	81	18	
27	3581.7	Ly $\alpha$	1216	1.946252	378	$6.5 \cdot 10^{13}$	$2.2 \cdot 10^{13}$	144	77	
28	3608.1	Ly $\alpha$	1216	1.968026	277	$3.2 \cdot 10^{13}$	$3.6 \cdot 10^{14}$	94	365	
29	3609.0	Ly $\alpha$	1216	1.968695	141	$7.8 \cdot 10^{14}$	$2.2 \cdot 10^{16}$	34	245	
30	3619.1	Ly $\alpha$	1216	1.977030	74	$6.1 \cdot 10^{14}$	$2.6 \cdot 10^{15}$	39	39	
31	3630.5	Ly $\alpha$	1216	1.986399	185	$4.9 \cdot 10^{13}$	$5.0 \cdot 10^{13}$	28	65	
32	3635.8	Ly $\alpha$	1216	1.990755	190	$5.3 \cdot 10^{13}$	$3.8 \cdot 10^{14}$	17	117	
33	3639.2	Ly $\alpha$	1216	1.993598	288	$4.3 \cdot 10^{13}$	$1.4 \cdot 10^{13}$	86	53	
34	3643.5	Si III	1206	2.019876	85	$2.4 \cdot 10^{14}$	$4.3 \cdot 10^{15}$	25	74	2
35	3646.7	Ly $\alpha$	1216	1.999757	338	$2.1 \cdot 10^{13}$	$5.5 \cdot 10^{13}$	19	190	
36	3651.1	Si II	1260	1.896765	47	$3.4 \cdot 10^{14}$	$2.9 \cdot 10^{13}$	99	6	1
37	3658.3	Ly $\alpha$	1216	2.009262	227	$3.1 \cdot 10^{13}$	$3.1 \cdot 10^{13}$	26	87	
38	3663.3	Ly $\alpha$	1216	2.013396	107	$7.9 \cdot 10^{13}$	$2.0 \cdot 10^{15}$	21	353	
39	3663.4	Ly $\alpha$	1216	2.013484	631	$1.6 \cdot 10^{14}$	$2.5 \cdot 10^{15}$	32	193	
40	3670.7	Ly $\alpha$	1216	2.019506	66	$2.3 \cdot 10^{15}$	$4.2 \cdot 10^{15}$	88	28	2
41	3676.6	Ly $\alpha$	1216	2.024317	178	$9.3 \cdot 10^{13}$	$1.7 \cdot 10^{13}$	101	32	
42	3705.2	Ly $\alpha$	1216	2.047883	276	$2.9 \cdot 10^{13}$	$1.1 \cdot 10^{13}$	53	61	
43	3708.9	Ly $\alpha$	1216	2.050899	126	$1.8 \cdot 10^{14}$	$4.0 \cdot 10^{15}$	16	98	
44	3717.3	Ly $\alpha$	1216	2.057789	179	$5.8 \cdot 10^{13}$	$4.2 \cdot 10^{14}$	17	108	
45	3724.6	Ly $\alpha$	1216	2.063838	224	$9.3 \cdot 10^{13}$	$1.2 \cdot 10^{16}$	9	331	
46	3729.1	Ly $\alpha$	1216	2.067530	79	$2.7 \cdot 10^{14}$	$3.6 \cdot 10^{13}$	95	12	
47	3735.5	Ly $\alpha$	1216	2.072811	101	$6.2 \cdot 10^{14}$	$1.0 \cdot 10^{14}$	140	16	
48	3738.7	Ly $\alpha$	1216	2.075420	119	$5.9 \cdot 10^{14}$	$6.8 \cdot 10^{15}$	30	72	
49	3742.0	Ly $\alpha$	1216	2.078157	139	$5.9 \cdot 10^{13}$	$1.4 \cdot 10^{13}$	47	36	
50	3772.9	Ly $\alpha$	1216	2.103547	58	$1.8 \cdot 10^{15}$	$2.7 \cdot 10^{15}$	80	24	
51	3778.5	Si II	1304	1.896765	47	$3.4 \cdot 10^{14}$	$2.9 \cdot 10^{13}$	99	6	1
52	3784.5	Si III	1206	2.136743	59	$6.5 \cdot 10^{13}$	$4.0 \cdot 10^{13}$	48	15	3
53	3789.0	Ly $\alpha$	1216	2.116801	70	$3.3 \cdot 10^{14}$	$2.4 \cdot 10^{15}$	27	49	
54	3794.1	Ly $\alpha$	1216	2.121016	265	$3.3 \cdot 10^{13}$	$1.1 \cdot 10^{15}$	9	251	
55	3797.7	Ly $\alpha$	1216	2.123953	70	$8.9 \cdot 10^{14}$	$2.4 \cdot 10^{16}$	20	83	
56	3804.1	Ly $\alpha$	1216	2.129255	210	$2.9 \cdot 10^{13}$	$8.3 \cdot 10^{12}$	50	48	
57	3813.5	Ly $\alpha$	1216	2.136973	50	$4.8 \cdot 10^{15}$	$1.6 \cdot 10^{16}$	66	30	3
58	3818.1	Ly $\alpha$	1216	2.140702	81	$1.6 \cdot 10^{14}$	$1.7 \cdot 10^{13}$	82	14	
59	3821.3	Ly $\alpha$	1216	2.143393	94	$1.1 \cdot 10^{14}$	$2.6 \cdot 10^{14}$	26	48	
60	3825.4	Ly $\alpha$	1216	2.146729	163	$6.6 \cdot 10^{13}$	$1.1 \cdot 10^{13}$	100	29	
61	3838.9	Ly $\alpha$	1216	2.157844	274	$2.1 \cdot 10^{13}$	$1.2 \cdot 10^{13}$	29	106	

